Enhanced bearing fault diagnosis using integral envelope spectrum from spectral coherence normalized with feature energy

Bingyan Chen [a], Yao Cheng [a,*], Weihua Zhang [a], Fengshou Gu [b]

[a] State Key Laboratory of Traction Power, Southwest Jiaotong University, Chengdu 610031, China

[b] Centre for Efficiency and Performance Engineering, University of Huddersfield, Huddersfield HD1 3DH, UK

*Corresponding author

E-mail addresses: chenbingyan@my.swjtu.edu.cn (B. Chen), chengyao2015@my.swjtu.edu.cn (Y. Cheng), tpl@swjtu.edu.cn (W. Zhang), f.gu@hud.ac.uk (F. Gu).

Abstract

Enhanced envelope spectrum (EES) and improved envelope spectrum (IES) generated from spectral coherence (SCoh) are proven to be more robust fault detection tools than squared envelope spectrum (SES). However, EES cannot effectively detect the fault-induced components under strong interference noise and IES can only capture the information of a fault-sensitive resonance spectral frequency band. To overcome these problems, weighted combined envelope spectrum (WCES) from SCoh is proposed as a novel fault detector. WCES integrates the fault components distributed in multiple resonance frequency bands using normalized feature energy and removes the envelope spectrum slices with less fault information to exclude disturbance noises. The performance of WCES is validated using simulations and experiments and compared with the advanced envelope spectra. The results demonstrate that WCES can effectively detect bearing faults under strong interference noise and multiple resonances compared with the SES, EES and IES, and has potential application value in bearing diagnostics.

Keywords: Weighted combined envelope spectrum; improved envelope spectrum; IESFOgram; spectral coherence; bearing diagnostics

1. Introduction

Rolling element bearing is a core component that ensures the high-speed rotation of shafts or rotors in modern mechanical systems, such as train wheelsets, aero-engines and various production machines, and their damage or failure has an important impact on production, transportation and safety. Fault diagnosis is an effective means to prevent mechanical failures and improve economic benefits. Signal-based fault diagnosis methods can be divided into non-machine learning methods and machine learning methods. The machine learning-based methods, such as transfer learning [1,2], can effectively realize the classification and recognition of multiple faults, but require a large amount of sample data and labeling data. Among non-machine learning methods, statistical indicator-based methods that benefit from easy implementation are commonly used in bearing fault detection, such as kurtosis [3] and entropy [4,5], but they cannot accurately identify fault types and usually require some reference data. In contrast, the frequency domain methods can accurately identify the fault type and do not require reference data and a large amount of sample data. However, because the signatures induced by bearing defects are often contaminated by interference noises from outside and inside the machine [6–8], some signal processing techniques are usually used for feature extraction before demodulation spectrum analysis, such as empirical mode decomposition [9], singular value decomposition [10], deconvolution [11], autocorrelated envelopes [12] and morphological filtering [13].

Local damage on bearing components usually induces repetitive transient impulses with a specific

Nomenclature	
Anomalous Envelope Spectrum	AES
Ball Pass Frequency of Outer Race	BPFO
Ball Pass Frequency of Inner Race	BPFI
Combined Envelope Spectrum	CES
Combined Improved Envelope Spectrum	CIES
Diagnostic Feature	DF
Enhanced Envelope Spectrum	EES
Envelope Spectrum Slice	ESS
Envelope Spectrum Slice Weight	ESSW
Generalized Integrated Spectrum	GIS
Improved Envelope Spectrum	IES
Improved Envelope Spectrum via Feature Optimization-gram	IESFOgram
Normalized Feature Energy	NFE
Spectral Correlation	SC
Spectral Coherence	SCoh
Squared Envelope Spectrum	SES
Signal-to-Noise Ratio	SNR
Weighted Combined Envelope Spectrum	WCES
Weighted Enhanced Envelope Spectrum	WEES
Weighted Envelope Spectrum	WES

characteristic frequency in vibration signals (at constant rotating speed) [14]. Squared envelope spectrum (SES) is a well-established method for bearing diagnostics by revealing the defect-induced characteristic frequency and its harmonics, but it performs poorly under strong interference noise. An effective solution is to perform SES analysis only on the fault-related resonance frequency band instead of the full frequency band to eliminate the interference noise. Many frequency band selection approaches have been developed for mechanical fault diagnosis, such as blind methods [15–20] and targeted methods [21–24]. The comparison of different band selection techniques can be referred to [23,25,26]. A popular and representative method is the fast kurtogram developed in [15], which uses a filter bank with 1/3-binary tree structure to split the vibration signals into a group of filtered signals with different center frequencies and limited bandwidths and takes the kurtosis of the narrow-band filtered signal to determine a frequency band with rich fault components. However, the fast kurtogram tends to choose the impulsive frequency band instead of the fault-related frequency band when confronted with strong random impulses [16].

The vibration signals induced by bearing defects have been proved to be second-order cyclostationary (i.e., signals contain hidden periodicities), and an effective analysis tool is the spectral correlation (SC) or its normalized form, namely the spectral coherence (SCoh) [14,27,28]. The SC and SCoh are dual-frequency representations that can simultaneously reveal the carrier frequency and cyclic frequency (and its harmonics) induced by bearing defects. It has been proved that the spectrum sequence generated by integrating the SC over all spectral frequencies is equivalent to the Fourier transform result of the squared envelope of the analyzed signal [27], which indicates an alternative approach to obtain the envelope spectra. The SES and enhanced envelope spectrum (EES) [29] have been constructed by integrating SCoh in the full spectral frequency band and used for fault detection of

rotating machinery. The EES usually performs better than the SES in enhancing non-zero cyclic components, but it cannot effectively reveal the fault-induced components under strong interference noise. Therefore, the spectrum obtained by integrating the SCoh over a certain spectral frequency band with rich fault information, namely improved envelope spectrum (IES) [30], was suggested to enhance the fault-related cyclic components and perform fault detection [29]. The selection of informative spectral frequency band is naturally transformed into a key factor affecting the fault diagnosis performance. An informative band selection method using the ratio of L2 norm to L1 norm [31] was proposed to distinguish multiple informative spectral frequency bands of the SCoh for constructing fault-sensitive IESs, but the bandwidth is fixed instead of determined adaptively. Recently, an improved envelope spectrum via feature optimization-gram (IESFOgram) method [32] was developed to adaptively select a fault-sensitive spectral frequency band of the SCoh to obtain the optimal IES and performed well in fault detection of gearbox bearings [33–35]. The IESFOgram splits the full spectral frequency band of the SCoh into a 1/3-binary tree structure and uses a targeted feature estimated from the IES of the narrow band to identify an optimal spectral frequency band. However, when the fault information is distributed in multiple resonance frequency bands, the IES can only capture the information of a certain resonance frequency band instead of all the resonance frequency bands. Subsequently, the IESFOgram was extended to construct a weighting function along the spectral frequency to obtain the combined IES (CIES) [36] for integrating the fault components around multiple resonant frequencies. The CIES assigns different weights to the envelope spectrum slices (ESSs) of the SCoh participating in the construction, presenting a spectrum construction strategy different from the EES and IES. However, the fault-unrelated components in the ESSs with small weights may affect the identification of the fault components, due to the consideration of the full spectral frequency band.

To improve the performance of the SCoh-based envelope spectrum analysis, this paper proposes a novel envelope spectrum constructed from the SCoh as a bearing fault detector. The presented method integrates the fault components distributed in multiple resonance frequency bands and reduces the interference of the fault-unrelated frequency bands. The performance of the developed method is validated on the bearing datasets from simulations and experiments and compared with the advanced envelope spectra. To sum up, the main contributions of this work are as follows:

(1) A weighted combined envelope spectrum (WCES) without dividing the spectral frequency band is proposed by integrating the SCoh with a normalized weight that assesses the level of fault-related information in each ESS.

(2) A threshold is introduced into the construction of normalized weights to identify the informative ESSs, which enables the proposed WCES can integrate fault information distributed in multiple resonance frequency bands, and remove the ESSs with less useful information to exclude the fault-unrelated interferences.

(3) The efficiency of the developed WCES is demonstrated using the different simulation signals and experimental bearing datasets, and the comparative analyses with SES, EES and IES illustrate the advantages of the developed WCES in bearing diagnostics under multiple resonances.

The remainder of this article is arranged as follows. In Section 2, the basic theory of the advanced envelope spectra for bearing diagnostics is briefly reviewed, including the SES and EES based on the SCoh, and the IES and CIES based on the IESFOgram. Section 3 introduces the theoretical basis of the proposed WCES in detail. In Section 4, the bearing diagnostic capability of WCES is validated on the simulated signals with single and double resonance frequencies and is compared with the IESFOgram-based IES. Section 5 presents the results of the WCES and the IESFOgram-based IES on

the experimental bearing datasets. In Section 6, the main conclusions of this paper are summarized.

2. Review of envelope spectra based on the spectral coherence

This section reviews the basic theory of the envelope spectra based on the SCoh, including the SES, EES, and the IES and CIES obtained by the IESFOgram, and briefly discusses the characteristics and limitations of these methods.

2.1. SES and EES based on the spectral coherence

Let $x(t_n)$, $t_n = n/F_s, n = 0,1,\cdots,N-1$, be a bearing vibration signal, where F_s and N are the sampling rate and length, respectively. Assume that the bearing vibration signal $x(t_n)$ is second-order cyclostationary, its instantaneous autocorrelation function can be obtained as [29]:

$$R_x(t_n,\tau_m) = E\left\{x(t_n)x(t_n-\tau_m)^*\right\} \tag{1}$$

where $E\{\cdot\}$ is the expectation operator, $*$ is the complex conjugate, and $\tau_m = m/F_s$. The SC is defined as the two-dimensional Fourier transform of the $R_x(t_n,\tau_m)$ [29]:

$$S_x(\alpha,f) = \lim_{N\to\infty}\frac{1}{(2N+1)F_s}\sum_{n=-N}^{N}\sum_{m=-\infty}^{\infty}R_x(t_n,\tau_m)e^{-j2\pi n\frac{\alpha}{F_s}}e^{-j2\pi m\frac{f}{F_s}} \tag{2}$$

The fast SC estimator proposed in [29] is employed to calculate the SC in this study. Usually, the normalized version of the SC, namely the SCoh, is used in practical applications, and defined as follows [28]:

$$\gamma_x(\alpha,f) = \frac{S_x(\alpha,f)}{\sqrt{S_x(0,f)S_x(0,f-\alpha)}} \tag{3}$$

The magnitude of the SCoh is between 0 and 1. By integrating the SCoh over the full spectral frequency range, the SES is defined as follows [27]:

$$S^{SES}(\alpha) = \frac{1}{F_s/2}\left|\int_0^{F_s/2}\gamma_x(\alpha,f)df\right| \tag{4}$$

Integrating the modulus of SCoh along the spectral frequency axis, the EES is formulated as follows [29]:

$$S^{EES}(\alpha) = \frac{1}{F_s/2}\int_0^{F_s/2}\left|\gamma_x(\alpha,f)\right|df \tag{5}$$

The definitions of the SES and EES indicate that the SCoh can be interpreted as a set composed of a series of parallel envelope spectra at the discrete spectral frequencies, thus the slice spectrum of the SCoh at a specific spectral frequency can be called the envelope spectrum slice (ESS).

When the bearing components are damaged, the fault information is not uniformly distributed in the full spectral frequency band. Specifically, the fault-related components are mainly concentrated in the frequency bands around the resonance frequencies, while other frequency bands are mainly dominated by the interference components. Neither the SES nor EES consider the difference of the fault information in the ESSs and adopt an equal weight strategy in the global integration of the SCoh. Therefore, these two methods are easily interfered with strong background noise, resulting in poor fault detection performance.

2.2. IES and CIES based on the IESFOgram

The IES constructed by integrating the modulus of SCoh over a specific spectral frequency band was developed as an enhanced fault detection tool [29,30]. The IES based on the SCoh is defined as follows [30]:

$$S^{IES}(\alpha)=\frac{1}{f_2-f_1}\int_{f_1}^{f_2}\left|\gamma_x(\alpha,f)\right|df \tag{6}$$

where f_1 and f_2 denote the starting and ending frequencies of the selected spectral frequency range, respectively. The selection of these two spectral frequencies has a significant influence on the IES-based bearing diagnostics and needs to be carefully determined.

The IESFOgram [32] can adaptively select a fault-induced resonance spectral frequency band of the SCoh to construct an optimal IES. In this approach, the full spectral frequency range of SCoh, i.e., $[0,F_s/2]$, is firstly divided into a 1/3-binary tree structure, where a total of 2^l narrow bands with equal bandwidths can be obtained at the *l*th level, $l=0,1,1.6,2,2.6,3,\cdots$. Then, a series of IESs are constructed by the integration of SCoh over the narrow spectral frequency bands as candidates. For the *i*th narrow band at the *l*th level, $i=1,2,3,\cdots,2^l$, the resulting IES is formulated as:

$$S_{l,i}^{IES}(\alpha)=\frac{1}{F_s/2^{l+1}}\int_{F_s\cdot(i-1)/2^{l+1}}^{F_s\cdot i/2^{l+1}}\left|\gamma_x(\alpha,f)\right|df \tag{7}$$

Further, a diagnostic feature (DF) [32], as defined in Eq. (8), is utilized as an evaluation indicator to measure the fault information contained in this narrow spectral frequency band.

$$\kappa_{l,i}^{DF}=\sum_{h=1}^{H}\frac{S_{l,i}^{IES}(h\cdot f_m)}{\frac{1}{2f_b}\left[\int_{h\cdot f_m-f_b}^{h\cdot f_m+f_b}S_{l,i}^{IES}(\alpha)d\alpha-S_{l,i}^{IES}(h\cdot f_m)\right]} \tag{8}$$

where H indicates the maximum harmonic order considered, f_m is the fault frequency to be detected, and $2f_b$ denotes the width of a tolerance band around the *h*th harmonic to estimate the noise level. Following the recommendation in [32], f_b is set as 1/3 of the shaft rotating frequency in this paper. At last, a narrow candidate band with largest DF is identified as the most informative spectral frequency band and the corresponding IES is employed to perform bearing diagnostics.

As mentioned above, the IESFOgram only selects an optimal spectral frequency band to construct the IES. To integrate the fault components distributed in multiple resonance frequency bands, the CIES [36] was developed by giving proper weights to the ESSs when integrating the SCoh over the full spectral frequency range. The weighting function $NDF(f)$ is extracted from the DF values in the IESFOgram. The CIES is defined as the integration of the product of SCoh and $NDF(f)$ over the full spectral frequency band [36]:

$$S^{CIES}(\alpha)=\int_0^{F_s/2}NDF(f)\cdot\left|\gamma_x(\alpha,f)\right|df \tag{9}$$

The CIES assigns different weights to the ESSs of the SCoh, which is a significant improvement in comparison with the EES and IES. Similarly, a weighting function constructed by the autocorrelation function of the ESSs was proposed to improve the SCoh-based envelope spectrum and generated the weighted enhanced envelope spectrum (WEES) [37]. However, considering that the ESSs with smaller weights are mainly dominated by interference information, the global weighted integration of the SCoh tends to introduce interference components into the final CIES and WEES, which interferes with the identification of the fault-induced frequencies.

3. Weighted combined envelope spectrum

3.1. Generalized integrated spectrum

The EES, IES and CIES can be interpreted as the special forms of the generalized integrated spectrum (GIS), which is obtained by the integration of the SCoh with a general weighting function. The GIS is defined as follows [38]:

$$S^{GIS}(\alpha)=\int_0^{F_s/2}\psi(\alpha,f)\cdot\left|\gamma_x(\alpha,f)\right|df \tag{10}$$

where $\psi(\alpha,f)$ represents a general weighting function, $0\le\psi(\alpha,f)\le 1$. In [38], a two-dimensional weighting function was constructed using the SCoh of the historical data acquired from the healthy machine and then introduced into the GIS to obtain an anomalous envelope spectrum (AES) for rotating machine diagnostics. In this study, the elements of each ESS of the SCoh are given equal weights, thus the GIS can be simplified as:

$$S^{GIS}(\alpha)=\int_0^{F_s/2}\psi(f)\cdot\left|\gamma_x(\alpha,f)\right|df \tag{11}$$

where $0\le\psi(f)\le 1$ denotes the weight of the ESS of the SCoh at the spectral frequency f. The EES, IES, CIES and AES can be regarded as special cases of the GIS with a specific weighting function. The weighting functions and characteristics of these envelope spectra are summarized in Table 1. An illustration of the weighting functions of these envelope spectra is shown in Fig. 1.

Table 1. The weighting functions and characteristics of the EES, IES, CIES and AES.

Envelope spectrum	Weighting function	Characteristics
EES	$\psi(f)=2/F_s,\forall f\in[0,F_s/2]$	• Integration over the full spectral frequency band • Equal weights for all ESSs
IES	$\psi(f)=1/(f_2-f_1),\forall f\in[f_1,f_2]$ and $\psi(f)=0,\forall f\notin[f_1,f_2]$	• Integration over a specific spectral frequency band • Equal weights for informative ESSs
CIES	$\psi(f)=NDF(f),\forall f\in[0,F_s/2]$	• Integration over the full spectral frequency band • Variable weights for all ESSs
AES	$\psi(\alpha,f)$, $\alpha\in[0,\alpha_{\max}]$ and $f\in[0,F_s/2]$	• Two-dimensional weight • Variable weights for the elements of the SCoh

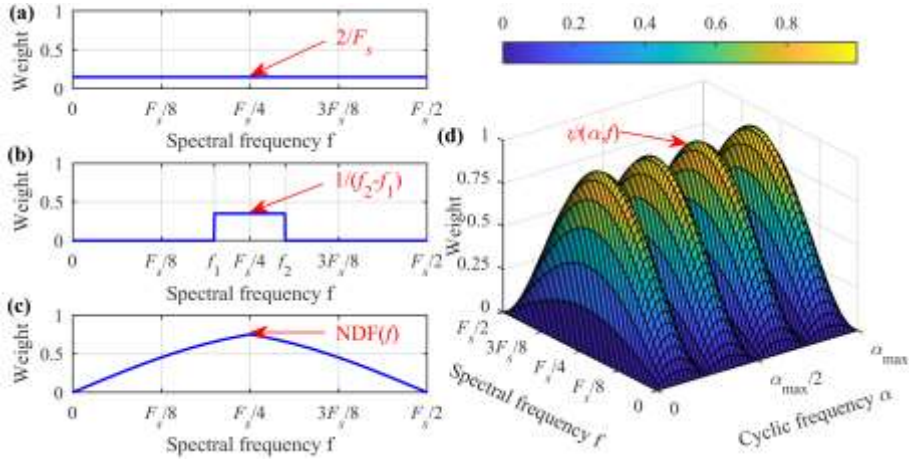

Fig. 1. Illustration of the weighting functions of typical envelope spectra: (a) EES, (b) IES, (c) CIES, and (d) AES.

3.2. Weighted combined envelope spectrum

The above analysis indicates that constructing an appropriate weighting function is essential to fully reveal the useful information of SCoh and boost the fault detection performance of GIS. To further improve the performance of the SCoh-based envelope spectra, this section introduces a novel weight function into the construction of GIS and proposes a novel WCES for bearing fault diagnostics.

For the ESS $S_x^k(\alpha)=\gamma_x(\alpha,f_k)$, $k=0,1,2,\cdots,N_w/2$, where N_w is the window length used for calculating the SCoh, a fault information measure, named the normalized feature energy (NFE), is used as the weight. The NFE is defined as the average energy of the characteristic frequencies of interest normalized by the average energy of all cyclic frequencies. For the *k*th ESS, its NFE is defined as:

$$\kappa_k^{NFE}=\frac{\frac{1}{H}\sum_{h=1}^{H}\max_{\alpha\in A_h}\left(\left|S_x^k(\alpha)\right|^2\right)}{\frac{1}{L}\sum_{i=1}^{L}\left|S_x^k(\alpha_i)\right|^2},A_h=\left\{\alpha\middle|h\cdot f_m-0.01f_m\le\alpha\le h\cdot f_m+0.01f_m\right\} \tag{12}$$

where f_m and H denote the detected fault frequency and its maximum harmonic order in the ESS, respectively. In this study, α_L is specified as the maximum cyclic frequency to scrutinize, and H is set as the maximum harmonic order of detected characteristic frequency in the range $[0,\alpha_L]$. The NFE-like metrics [39,40] have been used to measure the specific cyclostationary components in the frequency domain and show good performance.

By using the NFE to assess the level of fault-related information in ESS at each spectral frequency of the SCoh, the envelope spectrum slice weight (ESSW) is defined as:

$$w(f)=\frac{\frac{1}{H}\sum_{h=1}^{H}\max_{\alpha\in A_h}\left(\left|\gamma_x(\alpha,f)\right|^2\right)}{\frac{1}{L}\sum_{i=1}^{L}\left|\gamma_x(\alpha_i,f)\right|^2} \tag{13}$$

Based on the definition in Eq. (11), by integrating the SCoh with ESSW, the weighted envelope spectrum (WES) is proposed and defined as:

$$S^{WES}(\alpha)=\frac{\int_0^{F_s/2}w(f)\cdot\left|\gamma_x(\alpha,f)\right|df}{\int_0^{F_s/2}w(f)df} \tag{14}$$

To eliminate the interference components from the ESSs with small weights, the information threshold is introduced into the construction of the envelope spectrum. The information threshold is

defined as:

$$thres = \mu\left(w(f)\right) + \eta \cdot \sigma\left(w(f)\right) \tag{15}$$

where $\mu(\cdot)$ and $\sigma(\cdot)$ are respectively employed to calculate the mean and standard deviation, η is a non-negative coefficient used for adjusting the threshold.

By setting an appropriate threshold (equivalent to the coefficient η) and discarding the ESSs whose weights are lower than the threshold, the ESSW can be defined as:

$$w'(f) = \begin{cases} 0, & w(f) < thres \\ 1, & w(f) \geq thres \end{cases} \tag{16}$$

Based on the SCoh and modified ESSW, the combined envelope spectrum (CES) is proposed and defined as:

$$S^{CES}(\alpha) = \frac{\int_0^{F_s/2} w'(f) \cdot \left|\gamma_x(\alpha, f)\right| df}{\int_0^{F_s/2} w'(f) df} \tag{17}$$

The main difference between the IES and CES is that the former only focuses on the fault components in a specific spectral frequency band, while the latter integrates the fault information distributed in multiple spectral frequency bands. Thus CES is expected to achieve better performance than the IES when analyzing the vibration signal induced by multiple resonances. The explanation of the multiband combined envelope is presented in Appendix.

In addition, taking both information threshold and different weights into consideration, the ESSW defined in Eq. (13) can be modified as:

$$w''(f) = \begin{cases} 0, & w(f) < thres \\ w(f), & w(f) \geq thres \end{cases} \tag{18}$$

Based on the SCoh and improved ESSW, the WCES is further proposed and defined as:

$$S^{WCES}(\alpha) = \frac{\int_0^{F_s/2} w''(f) \cdot \left|\gamma_x(\alpha, f)\right| df}{\int_0^{F_s/2} w''(f) df} \tag{19}$$

A schematic description of the conventional envelope spectrum methods (SES, EES and IES) and novel envelope spectrum methods (WES, CES and WCES) for bearing diagnostics is shown in Fig. 2.

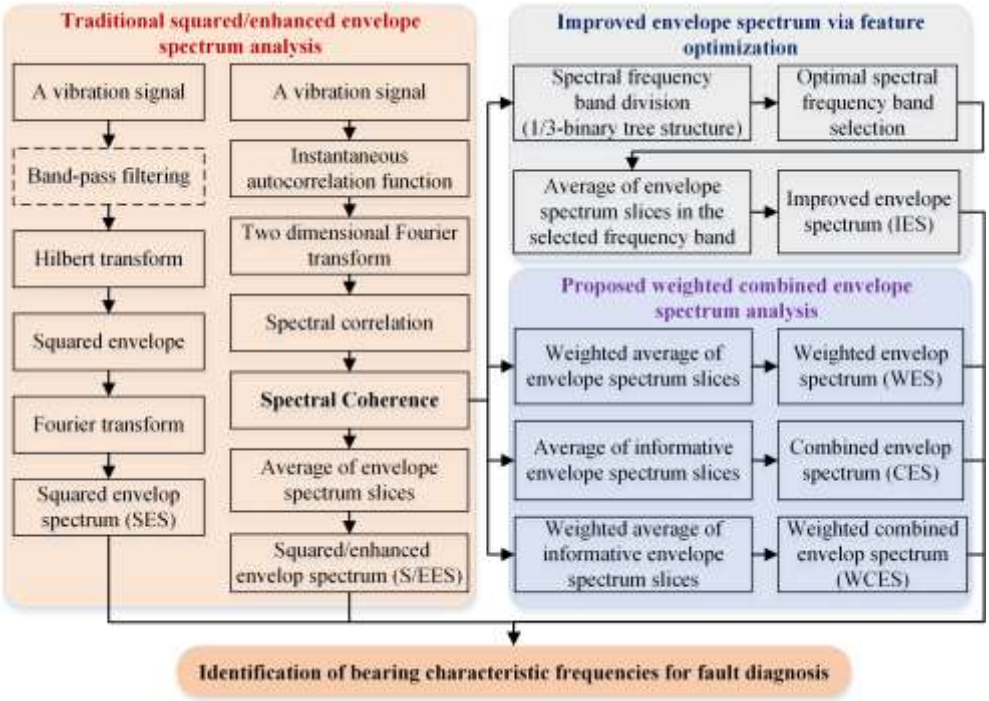

Fig. 2. Schematic description of the conventional and novel envelope spectrum methods for bearing diagnostics.

3.3. Selection of input parameters

The input parameters need to be specified before estimating the SCoh of the signal and performing the CES, WCES and IES analysis. The parameters of the SCoh include the window length and maximum observed cyclic frequency. The window length should be much smaller than the signal length while ensuring the desired spectral frequency resolution [29]. The cyclic frequency to scrutinize needs to include a minimum of three harmonics of the detected fault frequency for accurate diagnostics. The parameter of the CES and WCES is the coefficient η in the threshold. A small η means that more ESSs are used to construct the CES and WCES, but the resulting spectrum may contain more interference components; although a large η can improve the fault detection performance (note that the coefficient selected should ensure that at least one ESS is used to construct the CES and WCES), it cannot fully integrate the fault components in multiple resonance frequency bands. Therefore, the selection of the η should comprehensively consider the fault detection performance under single and multiple resonances. In this work, the window length is specified as 128 sampling points; the coefficient η is specified as 1.5 for the CES and WCES; for the IESFOgram, the decomposition level of the spectral frequency band is set to 6.

4. Verification with simulated bearing data

In this section, the fault detection performance of the WES, CES and WCES is verified on the simulated signals with single and double resonance frequencies, and compared with the SES based on Hilbert demodulation transform, EES based on the SCoh and IES based on the IESFOgram.

4.1. Model of simulated bearing data

Based on the vibration modal in [19,24], the following numerical model is established to generate the simulated bearing fault datasets:

$$x(t)=b(t)+r(t)+h(t)+n(t) \tag{20}$$

The first part $b(t)$ represents the repetitive impulse features induced by a local defect on bearing components and is usually simulated by the oscillating attenuation function [24]. The bearing fault component with single resonance frequency can be formulated as:

$$b(t)=\sum_{i=1}^{M_1} A_i \cdot e^{-2\pi\xi_1 f_{n,1}(t-i/f_m-\delta_i)} \sin\left(2\pi\sqrt{1-\xi_1^2}\, f_{n,1}\left(t-i/f_m-\delta_i\right)\right) \tag{21}$$

where M_1 denotes the total number of impulses with a repetition frequency of f_m in the sampling length; A_i represents the amplitude of the *i*th fault impulse and is specified as $A_i=1$ for outer race fault and $A_i=\left(1-\cos\left(2\pi f_r t\right)\right)/2$ for inner race fault, f_r being the shaft rotation frequency; $f_{n,1}$ and ξ_1 are the resonance frequency and damping ratio of bearing fault impulses, respectively; δ_i denotes the tiny fluctuation of the occurrence time of the *i*th fault impulse due to roller sliding and is generated from a uniform distribution $U\left(1/f_m, 2/f_m\right)/100$.

The bearing fault component with double resonance frequencies can be formulated as:

$$b(t)=\sum_{i=1}^{M_1} A_i \cdot e^{-2\pi\xi_1 f_{n,1}(t-i/f_m-\delta_i)} \cdot \sum_{s=1}^{2} \sin\left(2\pi\sqrt{1-\xi_1^2}\, f_{n,s}\left(t-i/f_m-\delta_i\right)\right) \tag{22}$$

where $f_{n,2}$ represents the second resonance frequency of the faulty bearing structure. Table 2 exhibits the specific parameters of simulated bearing outer and inner race fault impulse components.

The second part $h(t)$ denotes the discrete harmonics from the shaft rotation [19], and is defined as the sum of sinusoidal components:

$$h(t)=\sum_{j=1}^{M_2} B_j \cdot \sin\left(2\pi f_j t+\varphi_j\right) \tag{23}$$

where M_2 is the total number of interference harmonics; f_j, φ_j and B_j are the frequency, initial phase and amplitude of the *j*th harmonic interference. The parameters of simulated discrete harmonic interference component are presented in Table 3.

Table 2. Parameters of simulated bearing outer and inner race fault impulse components.

Parameter	M_1	f_m (Hz)	f_r (Hz)	$f_{n,1}$ (Hz)	$f_{n,2}$ (Hz)	ξ_1
Outer race fault	219	73	10	5800	1900	0.02
Inner race fault	291	97				

Table 3. Parameters of simulated discrete harmonic component.

Parameter	M_2	B_1	B_2	f_1 (Hz)	f_2 (Hz)	φ_1	φ_2
Value	2	0.05	0.05	10	20	$\pi/6$	$-\pi/3$

The third part $r(t)$ stands for the random impulses induced by the external impacts [19] and is also simulated using the oscillating attenuation function as:

$$r(t)=\sum_{k=1}^{M_3} C_k \cdot e^{-2\pi\xi_3 f_{n,3}(t-\tau_k)} \sin\left(2\pi\sqrt{1-\xi_3^2}\, f_{n,3}\left(t-\tau_k\right)\right) \tag{24}$$

where M_3 denotes the number of interference impulses and is specified as 5 in this study; C_k and τ_k indicate the magnitude and excitation time of the *k*th random impulse, and obtained by a normal distribution $N(5,1)$ and a uniform distribution $U(0,3)$, respectively; $f_{n,3}$ and ξ_3 are the

resonance frequency and damping ratio of random impulses, and are set to 10 kHz and 0.02, respectively.

The last part $n(t)$ is the background noise. In this study, the Gaussian white noise is added into the bearing fault component to give a signal-to-noise ratio (SNR) of –18 dB. The sampling rate and duration are assumed as 25.6 kHz and 3 s, respectively. In this study, the simulation analysis and experimental analysis are executed on the MATLAB R2016b environment on a desktop computer with a processor of Intel(R) Core(TM) i7-7700 CPU 3.60 GHz. The analysis results of simulated bearing fault datasets are exhibited in the subsequent subsections.

4.2. Bearing outer race fault with single and double resonances

This section analyzes the bearing outer race fault signals with single resonance and double resonances, respectively. Fig. 3(a)-(d) display the simulated bearing signal components. The Gaussian white noise with an SNR of –18dB is mixed into the bearing fault components with single and double resonant frequencies, as shown in Fig. 3(e) and (f). For clear viewing, only 1 s of the signal waveform is displayed.

Fig. 4(a) depicts the simulated outer race fault signal with single resonance frequency. The fault impulse features are completely buried in strong noise components. The resonance frequency band can be observed around 5800 Hz in Fig. 4(b), but the SES in Fig. 4(c) cannot reveal the outer race fault characteristic frequency (BPFO) and its first two harmonics (marked with red dot line). The maximum cyclic frequency to scrutinize is set to 250 Hz to cover three harmonics of the detected characteristic frequency. The weak BPFO and its first two harmonics are able to be identified from the SCoh exhibited in Fig. 4(d). In the ESSW plotted in Fig. 4(e), an obvious peak can be observed around 5800 Hz, indicating that the developed method correctly identifies the resonance frequency band and measures the distribution of bearing fault information.

The EES, WES, CES and WCES of simulated outer race fault signal with single resonance frequency are displayed in Fig. 5. The peak at the BPFO cannot be detected in the EES, while the WES, CES and WCES clearly exhibit the large amplitudes at the BPFO and its first two harmonics. The CES achieves better fault detection performance than the WES, but not as good as the WCES, judging from the amplitudes of the BPFO and its two harmonics. These results show that the weighted average of SCoh and the removal of the ESSs containing less fault information are reasonable and effective in the construction of the envelope spectra. For comparison, the processing results of the IESFOgram on the same signal are exhibited in Fig. 6. A spectral frequency band centered at 5700 Hz is selected by the IESFOgram, and its weight is plotted in Fig. 6(b). The large amplitudes at the BPFO and its two harmonics can also be clearly detected in the resulting IES, as shown in Fig. 6(c). Therefore, the WES, CES, WCES and the IESFOgram-based IES obtain good results in detecting bearing outer race fault with single resonance.

Fig. 7(a) exhibits the bearing outer race fault signal with double resonance frequencies. The fault-related components are heavily contaminated by strong interference components. The two resonance frequency bands can be identified around 1900 Hz and 5800 Hz in the frequency spectrum in Fig. 7(b). The BPFO and its two harmonics cannot be detected directly from the SES and SCoh, as presented in Fig. 7(c) and (d). In the ESSW depicted in Fig. 7(e), two peaks can be clearly observed around 1900 Hz and 5800 Hz, respectively, indicating that the two resonance frequency bands containing the outer race fault components can be accurately identified using the presented method.

The EES, WES, CES and WCES of bearing outer race fault simulated signal with double

resonance frequencies are displayed in Fig. 8. The spectral lines at the BPFO and its two harmonics can be observed from the WES, CES and WCES, but cannot be identified in the EES. The amplitudes at the BPFO and its two harmonics in CES and WCES are more obvious than that in WES, reflecting the better performance of CES and WCES in noise elimination and fault information disclosure. Fig. 9 shows the processing results of the IESFOgram on the simulated bearing fault signal with double resonance frequencies. The IESFOgram only captures the resonance frequency band centered at 5700 Hz and ignores another resonance frequency band with a center frequency of 1700 Hz. In the resulting IES, although the spectral lines at the BPFO and its two harmonics can also be identified, the corresponding amplitudes are not as obvious as those in the CES and WCES, indicating that the CES and WCES achieve better results than the IES in detecting this bearing outer race defect with double resonances.

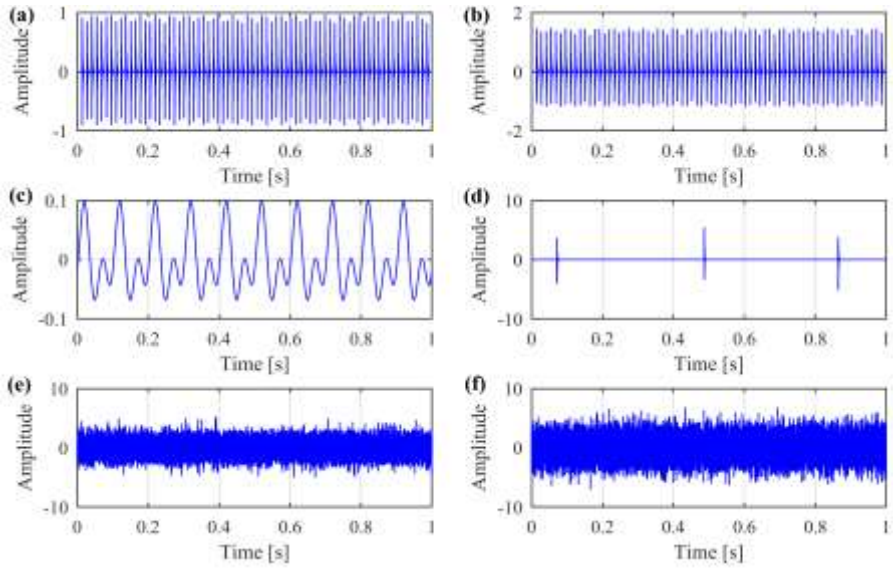

Fig. 3. Simulated signals of bearing outer race fault: (a) fault impulse component with single resonant frequency, (b) fault impulse component with double resonant frequency, (c) harmonic component, (d) random impulses, (e) mixed signal after adding the noise of –18dB to (a), and (f) mixed signal after adding the noise of –18dB to (b).

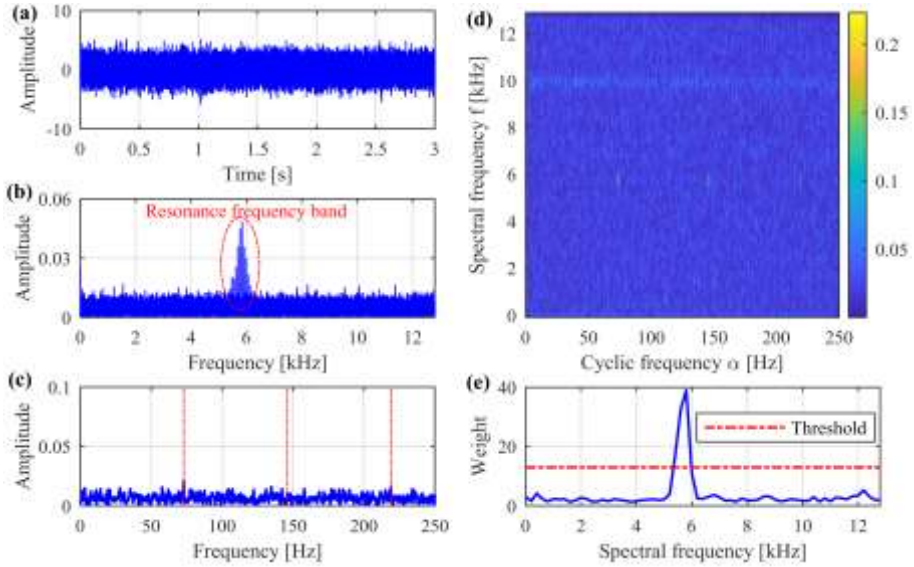

Fig. 4. Results of bearing outer race fault simulated signal with single resonant frequency: (a) waveform, (b)

frequency spectrum, (c) SES, (d) SCoh, and (e) ESSW.

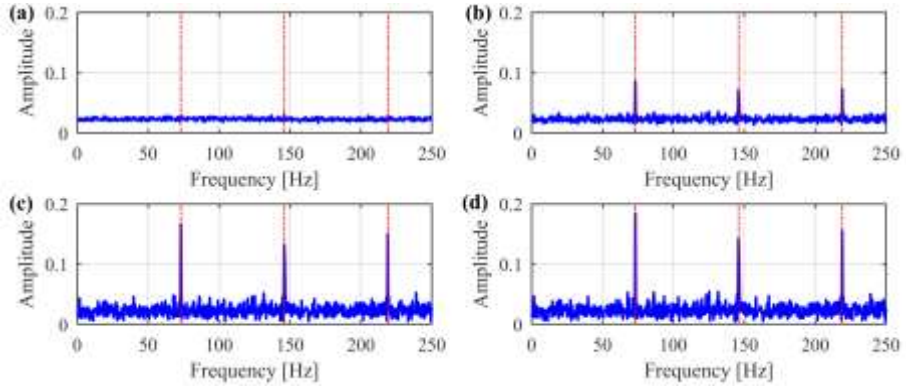

Fig. 5. Results of different envelope spectrum methods on the bearing outer race fault simulated signal with single resonant frequency: (a) EES, (b) WES, (c) CES, and (d) WCES.

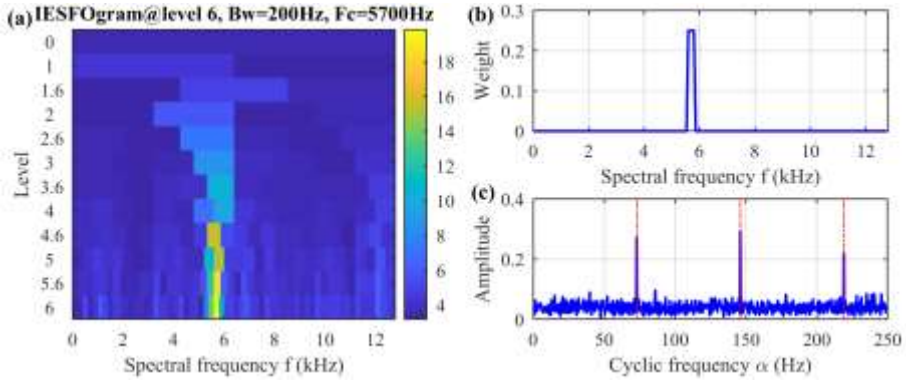

Fig. 6. Results of the IESFOgram on bearing outer race fault simulated signal with single resonant frequency: (a) IESFOgram, (b) weight of the selected frequency band, and (c) IES.

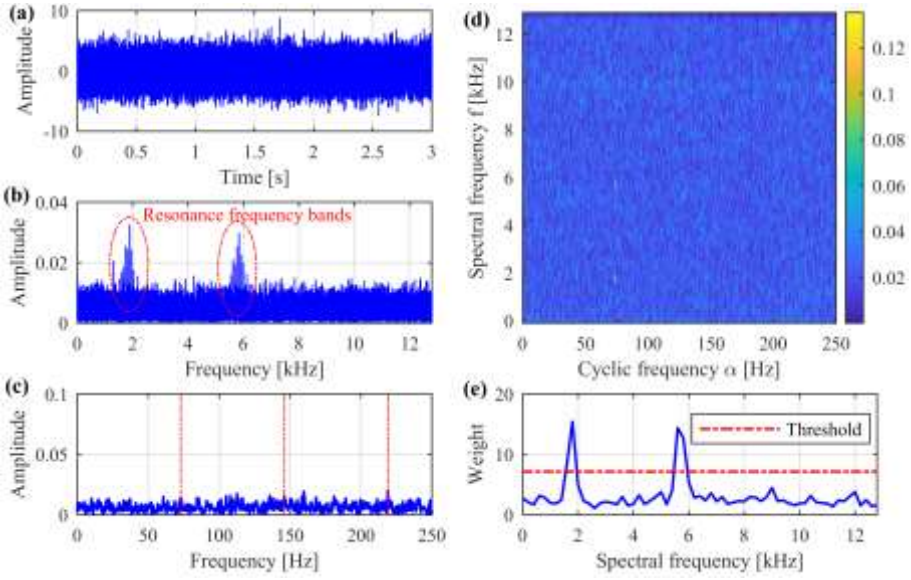

Fig. 7. Results of bearing outer race fault simulated signal with double resonant frequency: (a) waveform, (b) frequency spectrum, (c) SES, (d) SCoh, and (e) ESSW.

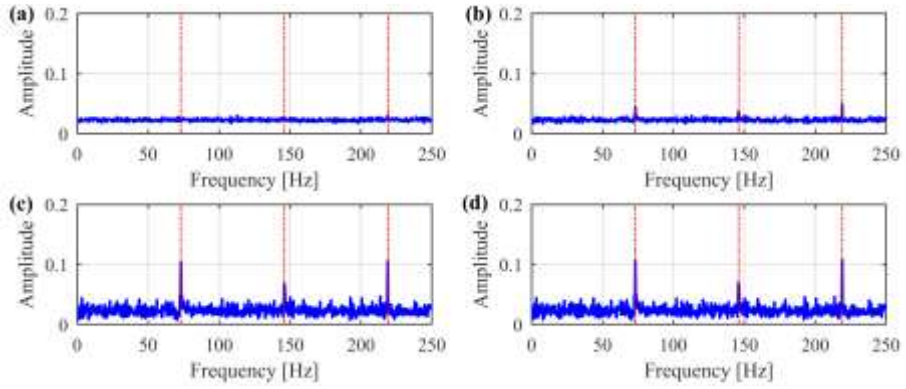

Fig. 8. Results of different envelope spectrum methods on the bearing outer race fault simulated signal with double resonant frequency: (a) EES, (b) WES, (c) CES, and (d) WCES.

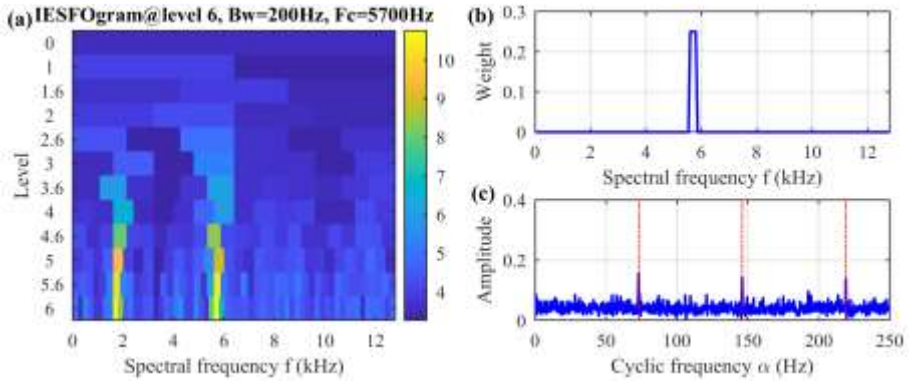

Fig. 9. Results of the IESFOgram on bearing outer race fault simulated signal with double resonant frequency: (a) IESFOgram, (b) weight of the selected frequency band, and (c) IES.

4.3. Bearing inner race fault with single and double resonances

This section analyzes bearing inner race fault simulated signals with single and double resonance frequencies, respectively. Fig. 10(a)-(d) display the simulated signal components related to bearing inner race fault. The Gaussian white noise with an SNR of –18dB is mixed into the bearing inner race fault components with single and double resonant frequencies, as presented in Fig. 10(e) and (f).

Fig. 11(a) shows the bearing inner race fault simulated signal with single resonance frequency. The inner race fault components are heavily polluted by the noise components, and only a few random impulses with large amplitudes are visible. In this section, the maximum observed cyclic frequency is specified as 350 Hz to cover three harmonics of the fault characteristic frequency of bearing inner race (BPFI). The resonance frequency band around 5800 Hz can be recognized in the frequency spectrum presented in Fig. 11(b), while the BPFI and its harmonics cannot be directly identified in the SES and SCoh, as displayed in Fig. 11(c) and (d). In the ESSW presented in Fig. 11(e), a peak can be clearly observed around 5800 Hz, indicating the good performance of the presented method in locating the spectral frequency band with rich fault information.

The EES, WES, CES and WCES of the same bearing fault simulated signal are displayed in Fig. 12. The spectral lines at the BPFI and its two harmonics cannot be observed from the EES but can be

clearly identified in the WES, CES and WCES. The apparent amplitudes at the bearing characteristic frequencies and the modulation sidebands indicate that the CES and WCES achieve similar results and are superior to the WES. It shows that the fault detection capability of the SCoh-based envelope spectrum can be enhanced significantly by removing the ESSs which contain less fault information. Fig. 13 shows the processing results of the IESFOgram on bearing fault simulated signal depicted in Fig. 11(a). The IESFOgram correctly identifies the resonance spectral frequency band around 5700 Hz with a bandwidth of 200 Hz. The BPFI and its two harmonics can also be determined in the resulting IES shown in Fig. 13(c), but their peaks are not as significant as those in the CES and WCES.

Fig. 14(a) depicts bearing inner race fault simulated signal with double resonance frequency. The fault impulse components are completely hidden in noisy interference components. In Fig. 14(b), the two resonance frequency bands around 1900 Hz and 5800 Hz can be recognized from the frequency spectrum. The BPFI and its harmonics are unable to be detected in the SES and SCoh, as displayed in Fig. 14(c) and (d). In the ESSW presented in Fig. 14(e), two dominant peaks can be easily discovered at the two resonance frequencies of the bearing inner race fault, indicating that the developed method is capable of quantifying the fault information distributed in multiple resonance frequency bands.

The EES, WES, CES and WCES of bearing inner race fault signal with double resonance frequency are exhibited in Fig. 15. The WES, CES and WCES exhibit large amplitudes at the BPFI and its two harmonics, while the EES is unable to capture the fault information of bearing inner race. The CES and WCES achieve similar fault detection results, and better than the WES. Fig. 16 displays the processing results of the IESFOgram on bearing fault simulated signal presented in Fig. 14(a). A resonance frequency band with a center frequency of 1700 Hz is selected by the IESFOgram, but another resonance frequency band around 5800 Hz is ignored, resulting in only the second harmonic of the BPFI can be identified from the resulting IES, as exhibited in Fig. 16 (c). Therefore, the CES and WCES achieve a better performance than the IES in detecting this bearing inner race fault with double resonances.

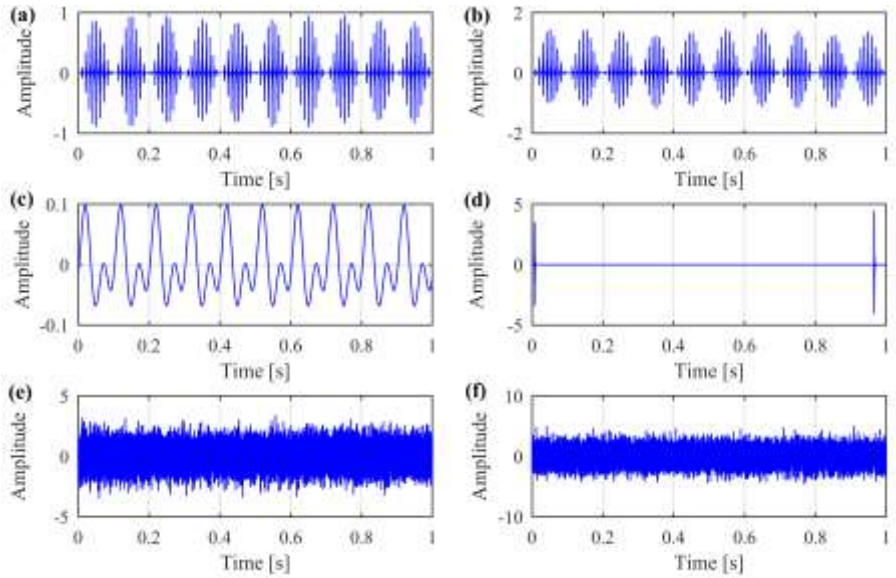

Fig. 10. Simulated signal of bearing inner race fault: (a) fault impulse component with single resonant frequency, (b) fault impulse component with double resonant frequency, (c) harmonic component, (d) random impulses, (e) mixed signal after adding the noise of –18dB to (a), and (f) mixed signal after adding the noise of –18dB to (b).

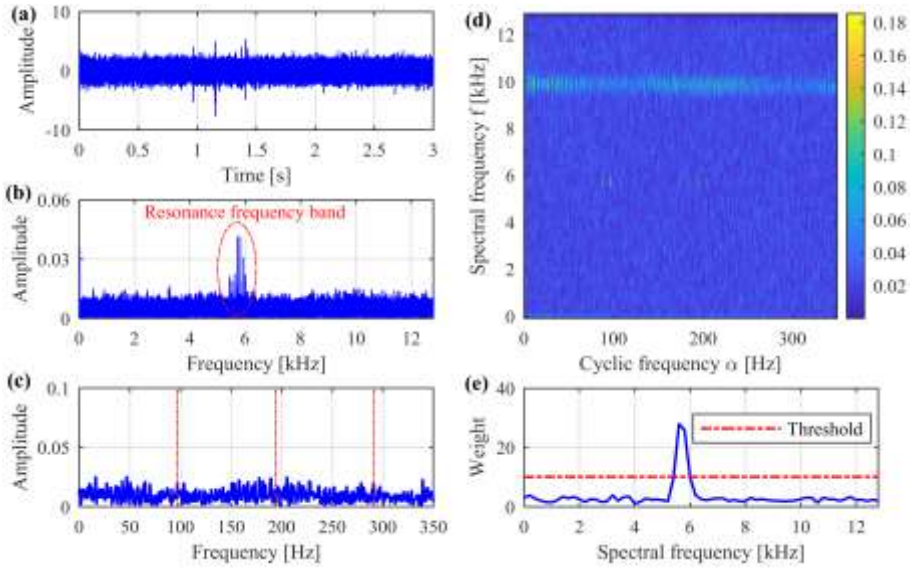

Fig. 11. Results of bearing inner race fault simulated signal with single resonant frequency: (a) waveform, (b) frequency spectrum, (c) SES, (d) SCoh, and (e) ESSW.

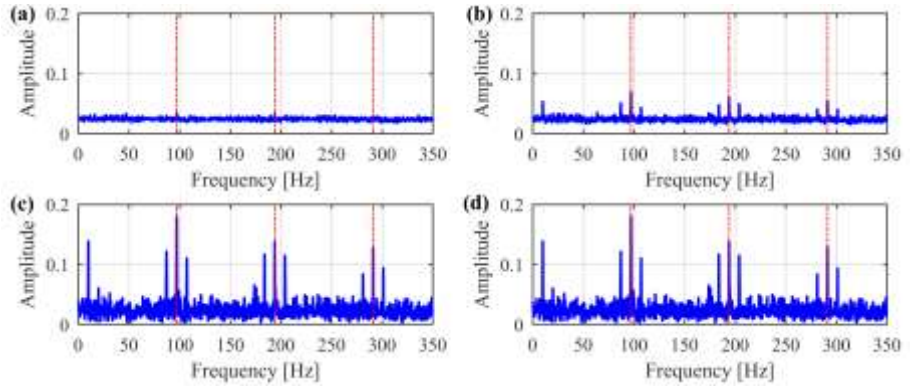

Fig. 12. Results of different envelope spectrum methods on the bearing inner race fault simulated signal with single resonant frequency: (a) EES, (b) WES, (c) CES, and (d) WCES.

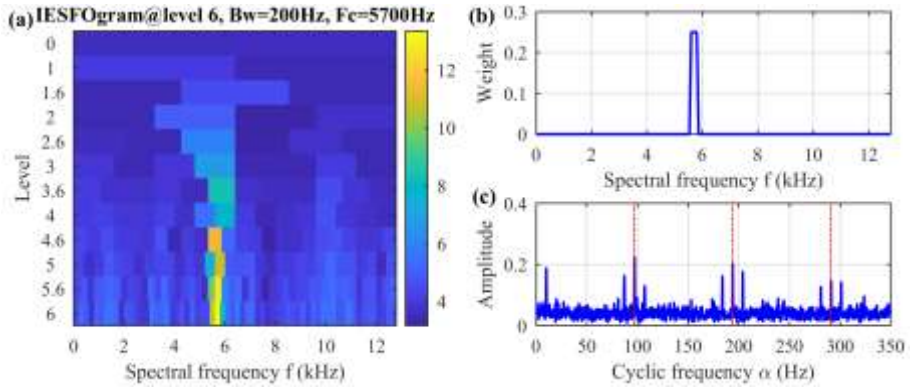

Fig. 13. Results of the IESFOgram on bearing inner race fault simulated signal with single resonant frequency: (a) IESFOgram, (b) weight of the selected frequency band, and (c) IES.

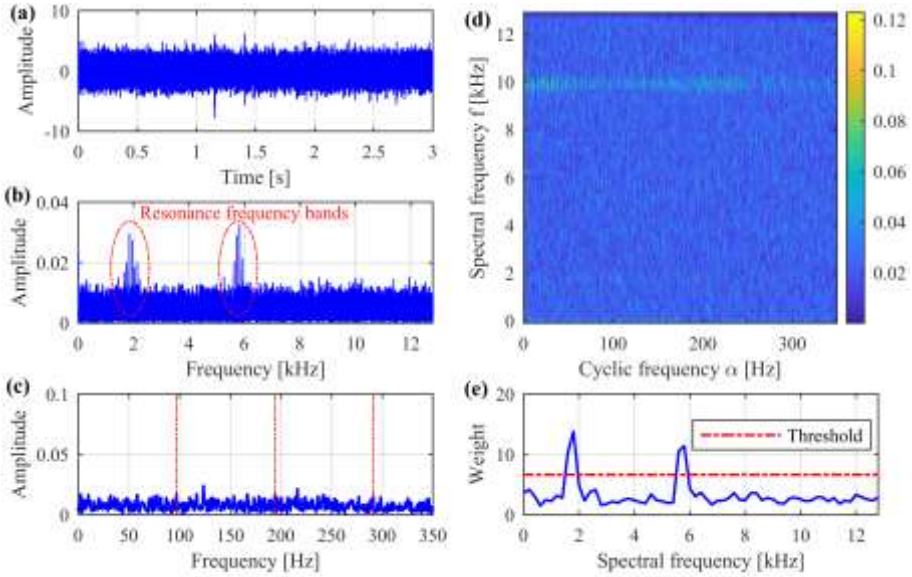

Fig. 14. Results of bearing inner race fault simulated signal with double resonant frequency: (a) waveform, (b) frequency spectrum, (c) SES, (d) SCoh, and (e) ESSW.

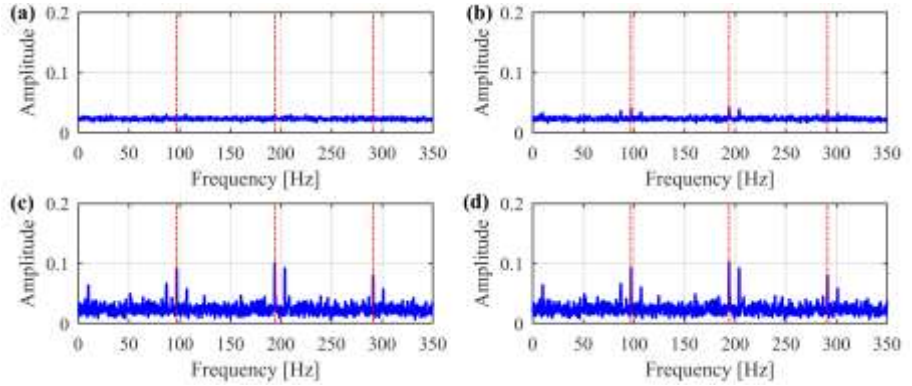

Fig. 15. Results of different envelope spectrum methods on the bearing inner race fault simulated signal with double resonant frequency: (a) EES, (b) WES, (c) CES, and (d) WCES.

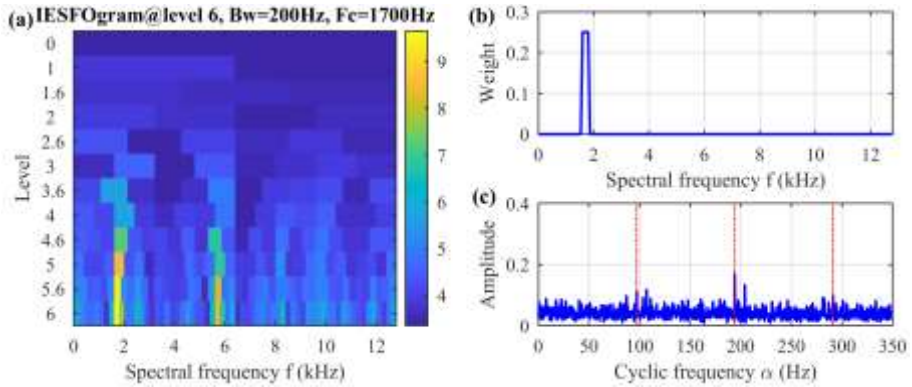

Fig. 16. Results of the IESFOgram on bearing inner race fault simulated signal with double resonant frequency: (a) IESFOgram, (b) weight of the selected frequency band, and (c) IES.

4.4. Performance analysis

This section evaluates quantitatively the performance of the conventional and proposed methods on the simulated bearing fault datasets. The previous analysis results show that the NFE can effectively measure the fault components in the envelope spectrum, so this paper continues to employ the NFE to quantitatively evaluate the fault extraction effects of different approaches.

Fig. 17 exhibits the NFE values of conventional and proposed envelope spectrum methods when processing the bearing fault simulated datasets. The NFE values calculated from the WES are greater than that of the EES and the NFE values of the CES are greater than that of the WES. It indicates that the ESSW is able to significantly improve the fault detection performance of the SCoh-based envelope spectrum, and the removal of the ESSs with less fault information is more effective than the weighted average in reducing interference noise. In addition, the NFE values of the WCES are greater than that of the IES, indicating that the WCES achieve better performance than the IES in identifying these bearing faults with single and double resonances.

Figs. 18 and 19 display the NFE values of the CES and WCES with different coefficients (equivalent to the thresholds) when analyzing the simulated signals of bearing outer race and inner faults, respectively. The NFE values of the CES and WCES increase with the increase of the coefficient and the difference between them decreases, indicating that the increase of the coefficient can simultaneously improve the performance of the CES and WCES and the effect of the weighting function on WCES is gradually insignificant. Furthermore, when the coefficient is higher than a specific value, the NFE values obtained by the CES and WCES are greater than that of the IESFOgram, especially when detecting bearing inner race faults, the CES and WCES with coefficients ranging from 0.5 to 3 exhibit better diagnostic performance than the IES. These results demonstrate the stronger cyclostationary detection capability of the developed WCES over the conventional envelope spectra, especially when analyzing bearing fault signals with more than one resonant frequency.

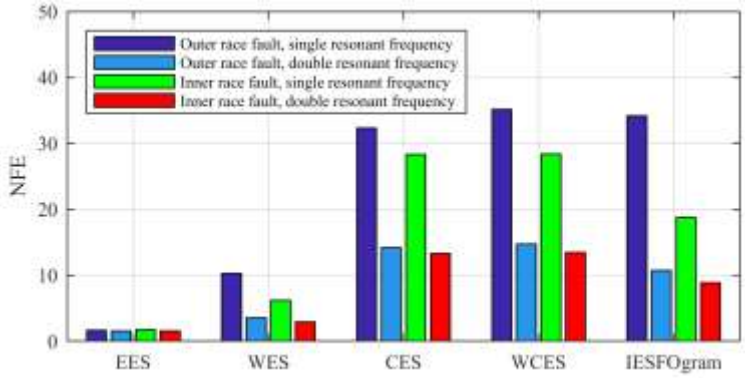

Fig. 17. NFE values obtained by conventional and proposed envelope spectra on bearing fault simulated signals.

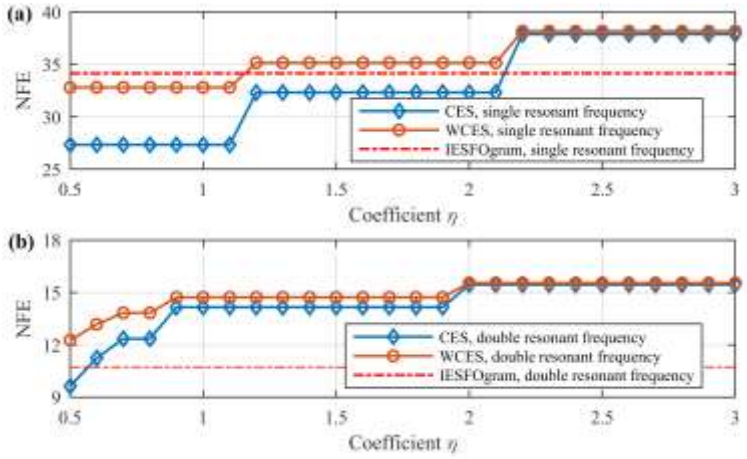

Fig. 18. NFE values of the CES and WCES with different coefficients on bearing outer race fault simulated signals.

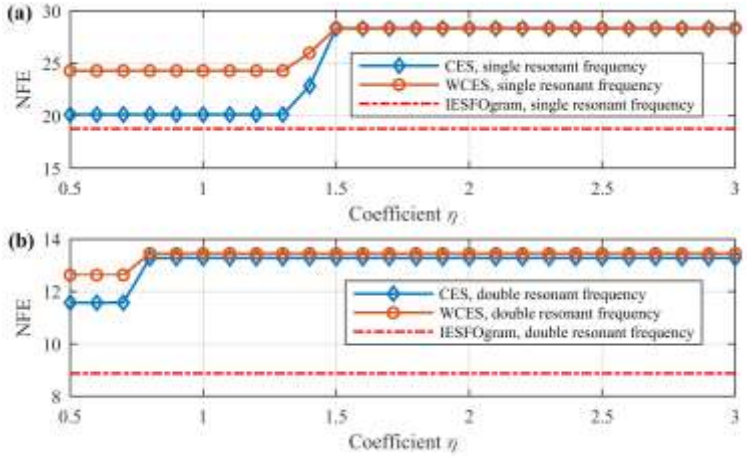

Fig. 19. NFE values of the CES and WCES with different coefficients on bearing inner race fault simulated signals.

5. Verification with experimental bearing data

This section utilizes two bearing experimental datasets (with single and multiple resonance frequencies, respectively) from two different test rigs to further verify the proposed envelope spectrum methods, and their performance is compared with the advanced envelope spectrum methods.

5.1. Case 1: Bearing outer race fault

The experimental data of outer race fault bearing [41] was collected from the planetary gearbox test rig of the University of New South Wales (UNSW), Australia. The tested gearbox mainly contains a parallel gear system, in which a spur gear integrated with the planet carrier is driven by a pinion, as shown in Fig. 20(a). An outer race defect was implanted into one planetary bearing (IKO model NAF 122812), as shown in Fig. 20(b). An acceleration sensor mounted above the stationary ring gear was used for the acquisition of vibration data with a sampling rate of 150 kHz. Data collection was carried out at a constant speed, and the rotation speed of the input shaft was about 324 r/min (5.4 Hz). The BPFO of planetary bearing is about 66.42 Hz, with modulation of 14.36 Hz. The maximum cyclic frequency to scrutinize is set to 250 Hz to cover three harmonics of the BPFO of planetary bearing.

The vibration signal of the tested planetary gearbox and its frequency spectrum are shown in Fig.

21(a) and (b), respectively. A series of transient impulses can be clearly discovered in the time-domain waveform, while the resonance frequency band is completely invisible in the frequency spectrum. Due to the strong interference noises, the BPFO and its harmonics are hardly identified directly in the SES and SCoh displayed in Fig. 21(c) and (d). An obvious peak can be observed around 47 kHz in the ESSW depicted in Fig. 21(e), indicating that the cyclic components related to bearing outer race fault are mainly distributed around this spectral frequency.

Fig. 22 displays the EES, WES, CES and WCES of the gearbox vibration signal. Similar to the SES, the EES and WES are unable to provide the information about the bearing outer race fault, while the CES and WCES confirm the outer race defect occurred on the planetary bearing by revealing the fault characteristic frequency 66.42 Hz and its harmonics (marked with red dot line). Fig. 23 exhibits the results of the IESFOgram for processing the same vibration signal. The spectral frequency band with a bandwidth of 1172 Hz and located at 47461 Hz is selected by the IESFOgram. In the resulting IES presented in Fig. 23(c), the spectral lines at the BPFO and its two harmonics can be identified, indicating that the IES also discovers the outer race defect of planetary bearing.

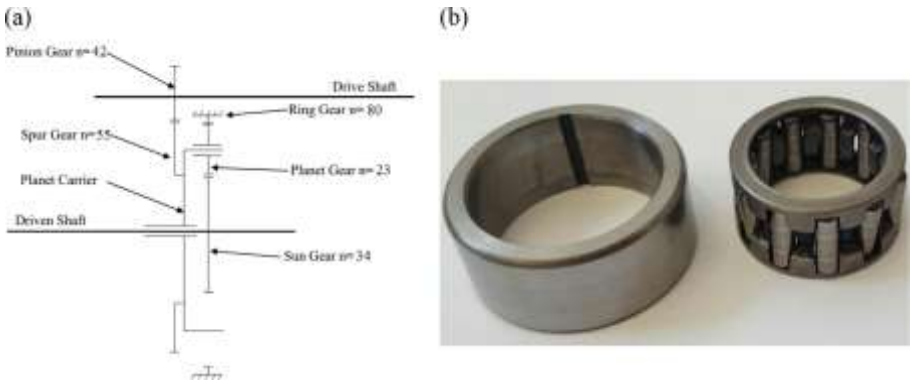

Fig. 20. (a) Diagram of the UNSW planetary gearbox test rig and (b) planetary bearing with seeded fault [23].

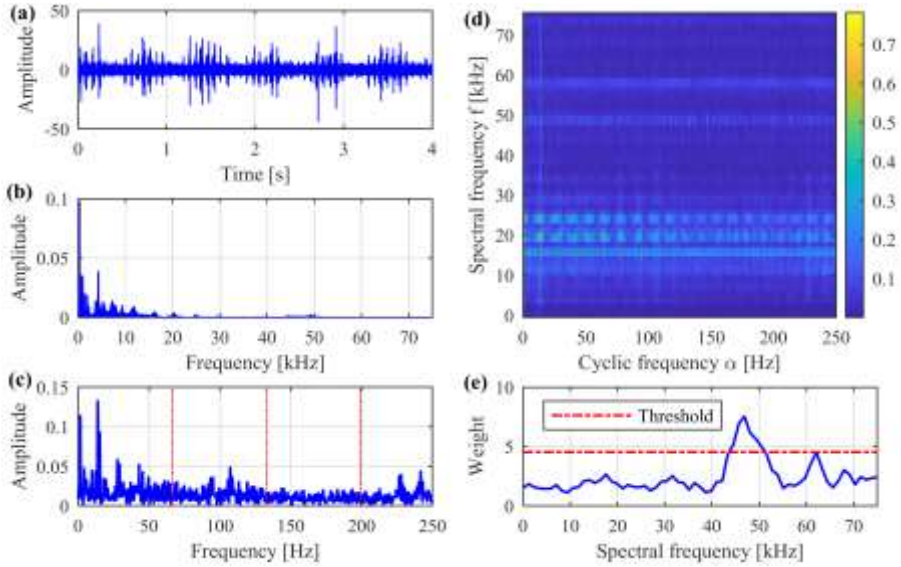

Fig. 21. Results of the planetary gearbox vibration data: (a) signal waveform, (b) frequency spectrum, (c) SES, (d) SCoh, and (e) ESSW.

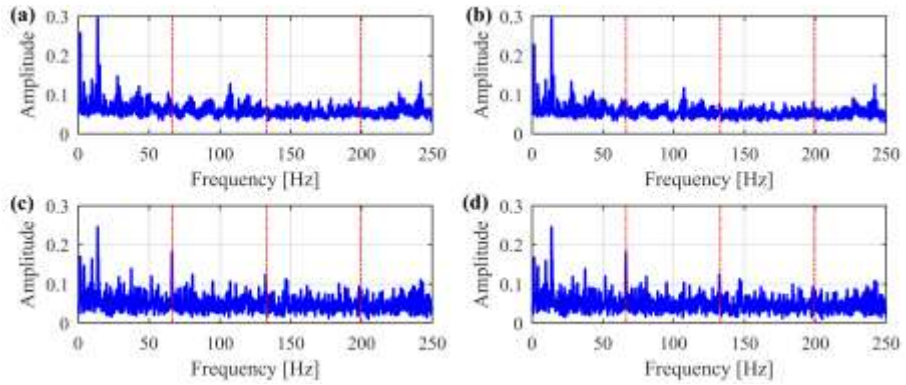

Fig. 22. Results of different envelope spectrum methods on the planetary gearbox vibration data: (a) EES, (b) WES, (c) CES, and (d) WCES.

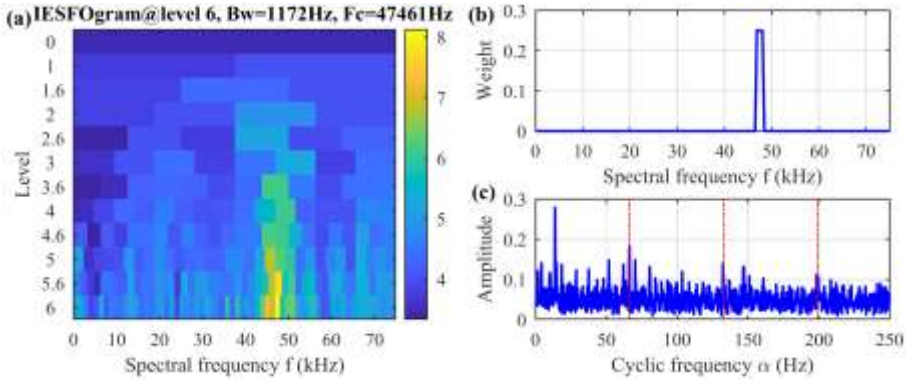

Fig. 23. Results of the IESFOgram method on the planetary gearbox vibration data: (a) IESFOgram, (b) weight of the selected frequency band, and (c) IES.

5.2. Case 2: Bearing inner race fault

The experimental data of inner race fault bearing [42] was collected from the bearing test rig of the University of Electronic Science and Technology of China (UESTC), China. The test rig is mainly composed of the motor and speed controller, support bearing, loading disc and test bearing, as exhibited in Fig. 24. A local defect was implanted into the inner race of the test bearing. The acceleration sensors were mounted on the housing of faulty bearing to record the bearing vibration data at a sampling rate of 51.2 kHz. The spindle rotated at a constant speed of 3600 r/min (60 Hz), and the BPFI of faulty bearing is about 325.8 Hz. In this case, the maximum observed cyclic frequency is specified as 1200 Hz to cover three harmonics of the BPFI.

Fig. 25(a) and (b) show the vibration signal and its frequency spectrum of inner race fault bearing, respectively. The resonance frequency bands cannot be directly identified in Fig. 25(b) because of the strong interference noises. The SES can barely discover the inner race damage of the bearing, judging from the weak amplitudes at the BPFI and its third harmonic, as depicted in Fig. 25(c). The SCoh displayed in Fig. 25(d) fails to reveal the BPFI of faulty bearing. In the ESSW shown in Fig. 25(e), three obvious peaks can be observed around 7 kHz, 11 kHz and 17.5 kHz, respectively, indicating that the cyclic components related to bearing inner race fault are mainly distributed around these three spectral frequencies.

Fig. 26 displays the EES, WES, CES and WCES of the experimental signal of bearing inner race fault. The BPFI and its two harmonics (marked with red dot line) can be detected in all the envelope spectra. The fault detection result of the EES is inferior to that of the WES, CES and WCES, and the CES and WCES achieve similar performance and are superior to the WES. Fig. 27 shows the results of the IESFOgram when analyzing the same vibration signal. A spectral frequency band located at 6600 Hz with a width of 400 Hz is selected by the IESFOgram to construct the IES. In Fig. 27(c), although the amplitudes at the BPFI and its two harmonics have been enhanced, many of the strong interference components are retained compared with the CES and WCES.

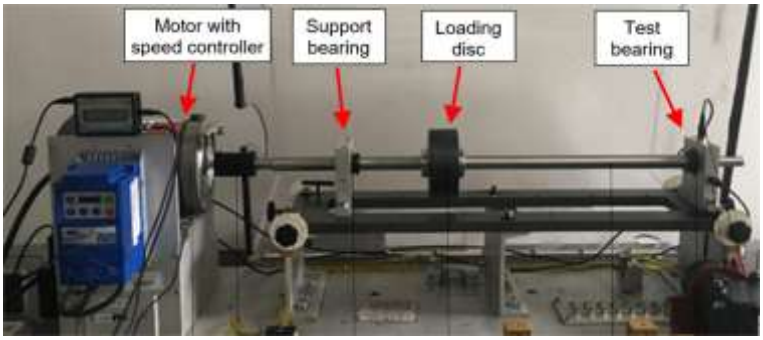

Fig. 24. UESTC bearing test rig [23].

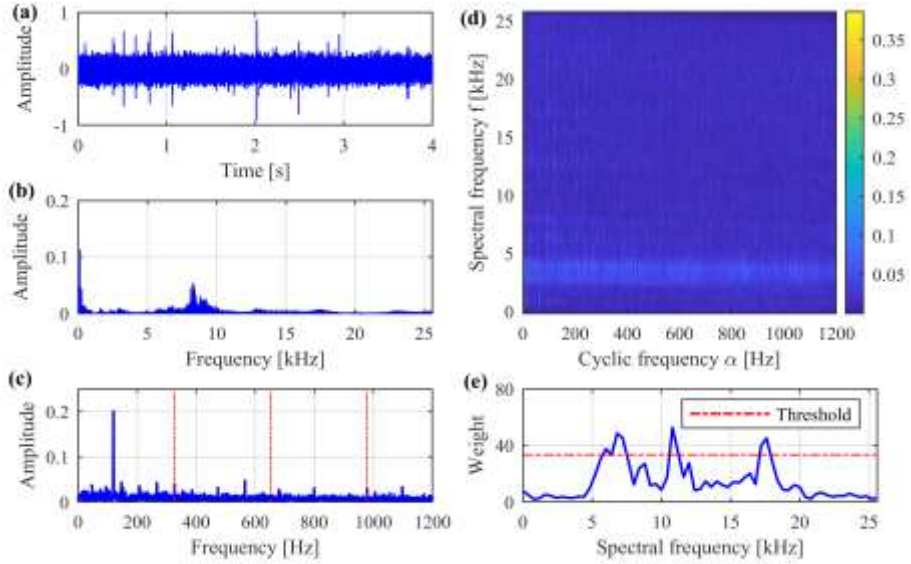

Fig. 25. Results of the vibration data of inner race fault bearing: (a) signal waveform, (b) frequency spectrum, (c) SES, (d) SCoh, and (e) ESSW.

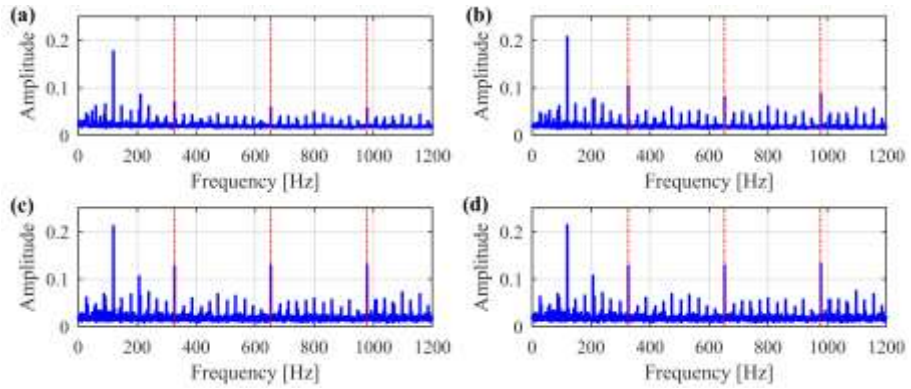

Fig. 26. Results of different envelope spectrum methods on the vibration data of inner race fault bearing: (a) EES, (b) WES, (c) CES, and (d) WCES.

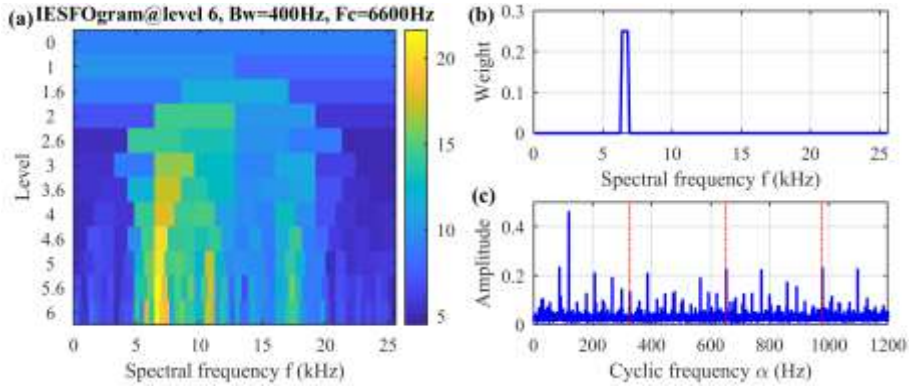

Fig. 27. Results of the IESFOgram method on the vibration data of inner race fault bearing: (a) IESFOgram, (b) weight of the selected frequency band, and (c) IES.

5.3. Performance analysis

This section evaluates the fault detection performance of the conventional and proposed envelope spectrum methods on the bearing experimental signals from a quantitative perspective.

Fig. 28 presents the NFE values of the conventional and presented methods on the bearing experimental signals. The CES and WCES have similar NFE values, which are greater than that of the WES, indicating the effectiveness of introducing the threshold strategy into the construction of ESSW. The CES, WCES and IESFOgram obtain similar NFE values when analyzing the vibration data of outer race fault bearing, but the NFE values of CES and WCES are significantly greater than that of the IESFOgram when analyzing the bearing inner race fault signal, reflecting better multi-resonance band detection performance than the IESFOgram.

Fig. 29 shows the NFE values obtained by the CES and WCES with different coefficients when processing the bearing experimental signals. It can be observed that the NFE values of the CES and WCES increase with the increase of the coefficient and the difference between them gradually disappears, which further indicates that their fault detection performance can be improved by increasing the coefficient, but the weighting function gradually loses its effect on the WCES. Similarly, when the coefficient is higher than a certain value, the NFE values of the CES and WCES are greater than that of the IESFOgram, especially when analyzing the vibration data of inner race fault bearing,

the CES and WCES with coefficients from 0.5 to 3 can achieve a higher NFE value than IESFOgram. These quantitative results again illustrate the efficiency and superiority of the WCES over the conventional envelope spectrum methods, especially in the analysis of bearing vibration datasets with multiple resonance frequencies.

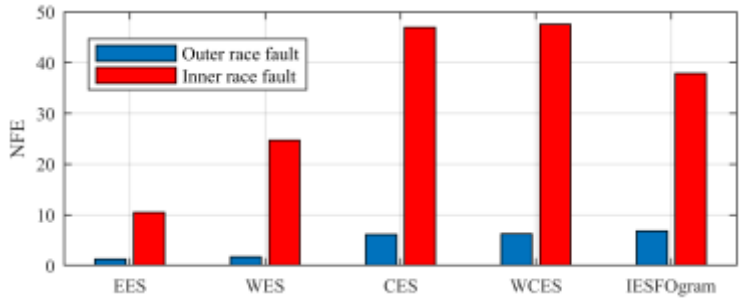

Fig. 28. NFE values obtained by conventional and proposed methods for experimental bearing signals.

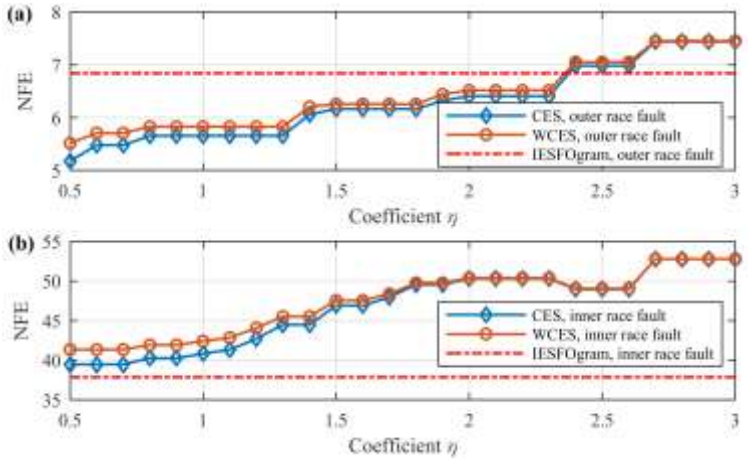

Fig. 29. NFE values obtained by the CES and WCES with different coefficients for experimental bearing signals.

6. Conclusions

How to construct an appropriate weighting function for the GIS to fully extract the fault-related cyclostationary features in the SCoh is still problematic. In this paper, a fault feature measure-based normalized weight that quantifies the diagnostic information level in each ESS is proposed to enhance the SCoh-based envelope spectrum analysis. An information threshold is introduced into the construction of normalized weight to preserve informative ESSs while reducing the interference components. Further, the WEC, CES and WCES are developed for cyclostationary analysis and bearing diagnostics. The simulations and experiments are conducted to validate the diagnostic capability of the proposed methods. Compared with the SES and EES, the WES, CES and WCES can effectively extract bearing fault features and reduce interference noise. Compared with the IESFOgram, the CES and WCES deliver good performance in integrating fault information distributed in multiple resonance frequency bands. The weighting function adopted by WCES can reveal fault features more effectively than the weighting functions adopted by WES and CES. Thus, the WCES is recommended for cyclostationary feature extraction and bearing diagnostics, and the recommended coefficient in threshold is higher than or equal to 1.5 by comprehensively analyzing the results under single and multiple resonance frequencies.

The proposed method is not really blind because it requires the fault characteristic frequency as input. Therefore, a weight estimation solution that does not rely on prior knowledge is worth studying in future work. In addition, the comparative analysis with other diagnostic techniques and the extension of the developed technique to the condition monitoring of rotating machinery components are also part of future work.

Acknowledgements

This work was supported by the Independent Research Project of State Key Laboratory of Traction Power, Southwest Jiaotong University, China (Grant No. 2021TPL-T11 and 2020TPL-T08). The authors would like to thank Dr. Wade A. Smith, Dr. Pietro Borghesani, Ms. Qing Ni, Dr. Kesheng Wang and Prof. Zhongxiao Peng for providing the bearing experimental data.

Appendix. Explanation of multiband combined envelope

Envelope analysis is usually only performed on the (squared) envelope of the band-pass filtered result around a resonance frequency. When the vibration signal is excited by multiple resonance frequencies, the (squared) envelopes of the filtered results on multiple resonance frequency bands can be integrated to fully extract useful information distributed on multiple resonance frequency bands.

Let $x(t)$ be a vibration signal with multiple resonance frequencies, the multi-band combined (squared) envelop signal is formulated as:

$$y(t) = a_{bp,1}(t) + a_{bp,2}(t) + \cdots + a_{bp,k}(t) = \sum_{n=1}^{k} a_{bp,n}(t) \tag{A1}$$

where $a_{bp,n}(t)$ denotes the (squared) envelope of the band-pass filtered result of the signal $x(t)$ around the nth resonance frequency, k the number of resonance frequencies.

Further, the spectrum of the multi-band combined (squared) envelope signal is expressed as:

$$\begin{aligned} &\int_{-\infty}^{\infty} y(t) e^{-j2\pi ft} dt = \int_{-\infty}^{\infty} \left(\sum_{n=1}^{k} a_{bp,n}(t) \right) e^{-j2\pi ft} dt \\ &= \int_{-\infty}^{\infty} a_{bp,1}(t) e^{-j2\pi ft} dt + \int_{-\infty}^{\infty} a_{bp,2}(t) e^{-j2\pi ft} dt + \cdots + \int_{-\infty}^{\infty} a_{bp,k}(t) e^{-j2\pi ft} dt \\ &= \sum_{n=1}^{k} \int_{-\infty}^{\infty} a_{bp,n}(t) e^{-j2\pi ft} dt \end{aligned} \tag{A2}$$

Eq. (A2) shows that the Fourier transform result of multi-band combined (squared) envelope signal obtained from the sum of several (squared) envelope signals is equivalent to the sum of the Fourier transform results of these (squared) envelope signals. Therefore, the combination of (squared) envelope spectra on multiple frequency bands can sufficiently extract useful information distributed in multiple frequency bands.

References

[1] Y. Zou, Y. Liu, J. Deng, Y. Jiang, W. Zhang, A novel transfer learning method for bearing fault diagnosis under different working conditions, Measurement 171 (2021) 108767.

[2] B. Yang, C.G. Lee, Y. Lei, N. Li, N. Lu, Deep partial transfer learning network: A method to selectively transfer diagnostic knowledge across related machines, Mech. Syst. Signal Process. 156 (2021) 107818.

[3] P. Poveda-Martínez, J. Ramis-Soriano, A comparison between psychoacoustic parameters and condition indicators for machinery fault diagnosis using vibration signals, Appl. Acoust. 166 (2020) 1–13.

[4] R. Yan, Y. Liu, R.X. Gao, Permutation entropy: A nonlinear statistical measure for status characterization of rotary machines, Mech. Syst. Signal Process. 29 (2012) 474–484.

[5] M. Rostaghi, M. Reza, H. Azami, Application of dispersion entropy to status characterization of rotary machines, J. Sound Vib. 438 (2019) 291–308.

[6] I.S. Bozchalooi, M. Liang, A joint resonance frequency estimation and in-band noise reduction method for enhancing the detectability of bearing fault signals, Mech. Syst. Signal Process. 22 (2008) 915–933.

[7] Y. Wang, M. Liang, An adaptive SK technique and its application for fault detection of rolling element bearings, Mech. Syst. Signal Process. 25 (2011) 1750–1764.

[8] W.A. Smith, Z. Fan, Z. Peng, H. Li, R.B. Randall, Optimised Spectral Kurtosis for bearing diagnostics under electromagnetic interference, Mech. Syst. Signal Process. 75 (2016) 371–394.

[9] Y.F. Hu, Q. Li, An adjustable envelope based EMD method for rolling bearing fault diagnosis, IOP Conf. Ser. Mater. Sci. Eng. 1043 (2021) 032017.

[10] L. Xu, S. Chatterton, P. Pennacchi, Rolling element bearing diagnosis based on singular value decomposition and composite squared envelope spectrum, Mech. Syst. Signal Process. 148 (2021) 107174.

[11] Y. Li, G. Cheng, C. Liu, Research on bearing fault diagnosis based on spectrum characteristics under strong noise interference, Measurement 169 (2021) 108509.

[12] Y. Xu, D. Zhen, J.X. Gu, K. Rabeyee, F. Chu, F. Gu, A.D. Ball, Autocorrelated Envelopes for early fault detection of rolling bearings, Mech. Syst. Signal Process. 146 (2020) 106990.

[13] B. Chen, D. Song, W. Zhang, Y. Cheng, Z. Wang, A performance enhanced time-varying morphological filtering method for bearing fault diagnosis, Measurement 176 (2021) 109163.

[14] R.B. Randall, J. Antoni, Rolling element bearing diagnostics-A tutorial, Mech. Syst. Signal Process. 25 (2011) 485–520.

[15] J. Antoni, Fast computation of the kurtogram for the detection of transient faults, Mech. Syst. Signal Process. 21 (2007) 108–124.

[16] T. Barszcz, A. Jabłoński, A novel method for the optimal band selection for vibration signal demodulation and comparison with the Kurtogram, Mech. Syst. Signal Process. 25 (2011) 431–451.

[17] P.W. Tse, D. Wang, The design of a new sparsogram for fast bearing fault diagnosis: Part 1 of the two related manuscripts that have a joint title as “two automatic vibration-based fault diagnostic methods using the novel sparsity measurement - Parts 1 and 2,” Mech. Syst. Signal Process. 40 (2013) 499–519.

[18] J. Antoni, The infogram: Entropic evidence of the signature of repetitive transients, Mech. Syst. Signal Process. 74 (2016) 73–94.

[19] Y. Miao, M. Zhao, J. Lin, Improvement of kurtosis-guided-grams via Gini index for bearing fault feature identification, Meas. Sci. Technol. 28 (2017) 125001.

[20] A. Moshrefzadeh, A. Fasana, The Autogram: An effective approach for selecting the optimal demodulation band in rolling element bearings diagnosis, Mech. Syst. Signal Process. 105 (2018) 294–318.

[21] P. Borghesani, P. Pennacchi, S. Chatterton, The relationship between kurtosis- and envelope-based indexes for the diagnostic of rolling element bearings, Mech. Syst. Signal Process. 43 (2014) 25–43.

[22] W.A. Smith, R.B. Randall, X. de C. du Mée, P. Peng, Use of cyclostationary properties to diagnose planet bearing faults in variable speed conditions, 10th DST Gr. Int. Conf. Heal. Usage Monit. Syst. 17th Aust. Aerosp. Congr. (2017) 26–28.

[23] W.A. Smith, P. Borghesani, Q. Ni, K. Wang, Z. Peng, Optimal demodulation-band selection for envelope-based diagnostics: A comparative study of traditional and novel tools, Mech. Syst. Signal Process. 134 (2019) 106303.

[24] Q. Ni, J.C. Ji, K. Feng, B. Halkon, A novel correntropy-based band selection method for the fault diagnosis of bearings under fault-irrelevant impulsive and cyclostationary interferences, Mech. Syst. Signal Process. 153 (2021) 107498.

[25] J. Hebda-Sobkowicz, R. Zimroz, A. Wyłomanska, Selection of the informative frequency band in a bearing fault diagnosis in the presence of non-gaussian noise-Comparison of recently developed methods, Appl. Sci. 10 (2020) 2657.

[26] D. Wang, Some further thoughts about spectral kurtosis, spectral L2/L1 norm, spectral smoothness index and spectral Gini index for characterizing repetitive transients, Mech. Syst. Signal Process. 108 (2018) 58–72.

[27] R.B. Randall, J. Antoni, S. Chobsaard, The relationship between spectral correlation and envelope analysis in the diagnostics of bearing faults and other cyclostationary machine signals, Mech. Syst. Signal Process. 15 (2001) 945–962.

[28] J. Antoni, Cyclic spectral analysis of rolling-element bearing signals: Facts and fictions, J. Sound Vib. 304 (2007) 497–529.

[29] J. Antoni, G. Xin, N. Hamzaoui, Fast computation of the spectral correlation, Mech. Syst. Signal Process. 92 (2017) 248–277.

[30] D. Abboud, J. Antoni, Order-frequency analysis of machine signals, Mech. Syst. Signal Process. 87 (2017) 229–258.

[31] D. Wang, X. Zhao, L.L. Kou, Y. Qin, Y. Zhao, K.L. Tsui, A simple and fast guideline for generating enhanced/squared envelope spectra from spectral coherence for bearing fault diagnosis, Mech. Syst. Signal Process. 122 (2019) 754–768.

[32] A. Mauricio, W.A. Smith, R.B. Randall, J. Antoni, K. Gryllias, Improved Envelope Spectrum via Feature Optimisation-gram (IESFOgram): A novel tool for rolling element bearing diagnostics under non-stationary operating conditions, Mech. Syst. Signal Process. 144 (2020) 106891.

[33] A. Mauricio, S. Sheng, K. Gryllias, Condition monitoring of wind turbine planetary gearboxes under different operating conditions, J. Eng. Gas Turbines Power. 142 (2020) 1–8.

[34] A. Mauricio, J. Qi, K. Gryllias, Vibration-based condition monitoring of wind turbine gearboxes based on cyclostationary analysis, J. Eng. Gas Turbines Power. 141 (2019) 1–8.

[35] A. Mauricio, J. Qi, W.A. Smith, M. Sarazin, R.B. Randall, K. Janssens, K. Gryllias, Bearing diagnostics under strong electromagnetic interference based on Integrated Spectral Coherence, Mech. Syst. Signal Process. 140 (2020) 106673.

[36] A. Mauricio, K. Gryllias, Cyclostationary-based Multiband Envelope Spectra Extraction for bearing diagnostics: The Combined Improved Envelope Spectrum, Mech. Syst. Signal Process. 149 (2021) 107150.

[37] J.H. Lee, A weighting function for improvement of spectral coherence based envelope spectrum, Mech. Syst. Signal Process. 160 (2021) 107929.

[38] S. Schmidt, K.C. Gryllias, The anomalous and smoothed anomalous envelope spectra for

rotating machine fault diagnosis, Mech. Syst. Signal Process. 158 (2021) 107770.

[39] X. Yan, Y. Liu, M. Jia, Research on an enhanced scale morphological-hat product filtering in incipient fault detection of rolling element bearings, Measurement 147 (2019) 106856.

[40] J. Hebda-Sobkowicz, R. Zimroz, M. Pitera, A. Wyłomańska, Informative frequency band selection in the presence of non-Gaussian noise – a novel approach based on the conditional variance statistic with application to bearing fault diagnosis, Mech. Syst. Signal Process. 145 (2020) 106971.

[41] W. Smith, P. Borghesani, Q. Ni, K. Wang, Z. Peng, Data5-1_Test1_ConstSpeed10sec_section.mat(https://www.researchgate.net/publication/337067239_Data5-1_Test1_ConstSpeed10sec_sectionmat), (2019).

[42] W. Smith, P. Borghesani, Q. Ni, K. Wang, Z. Peng, Data5-3_60Hz-inner.mat (https://www.researchgate.net/publication/337067159_Data5-3_60Hz-innermat), (2019).